Perforation of aluminium alloy thin plates

Léonard Antoinat, Régis Kubler, Jean-Luc Barou, Philippe Viot, Laurent Barrallier

Perforation of aluminium alloy thin plates

Léonard Antoinat [a, *], Régis Kubler [a], Jean-Luc Barou [b], Philippe Viot [b], Laurent Barrallier [a]

[a] MSMP Laboratory, Arts et Métiers ParisTech, 2 cours des Arts et Métiers, 13617 Aix en Provence, France
[b] I2M, Arts et Métiers ParisTech, UMR 5295, 33405 Talence, France

ARTICLE INFO

Article history:
Received 20 February 2014
Received in revised form
24 July 2014
Accepted 28 July 2014
Available online 16 September 2014

Keywords:
Perforation
Aluminum
Experiments
FE simulations
Analytical perforation model

ABSTRACT

Low velocity perforation of aeronautical aluminium alloy sheets 2024 T3 is studied in this paper. After a literature review on recent experiments and models of plate's perforation, experimental results for 2 thicknesses (2 mm and 4 mm) of plates are presented. Perforation tests are performed with an instrumented drop test. The striker has a large diameter and a conical shape nose. Two models for perforation are presented and calibrated to bring a better understanding of the experiments. The first one is an analytical model based on an energetic approach. The second one is a numerical shell Finite Element FE model. A Johnson Cook phenomenological behaviour law of the plate's material is implemented in the finite element code Abaqus/Explicit. The velocity, the evolution of the impact force, the absorbed energy and the cracks' propagation are analysed.

1. Introduction and literature review

Impact engineering is a common field in sectors as the nautical [33], the aeronautical [19], automotive industries [16] and in metalforming applications [28]. Perforation of thin plates by a conical nose striker is a particular case of impact because of the large deformation, the damage and the rupture of the plate. Various perforation tests can be performed with high [23] ($\geq$ 70 m/s) or low [32] ($\leq$5 m/s) initial velocities and with different striker's geometries. A typical approach for perforation is to study the variation of the velocity and to compare the residual velocity with the initial velocity of the striker. The ballistic limit velocity is defined as the minimal velocity needed to perforate the plate [4,17,23]. It is also possible to calculate the energy E_a absorbed by the plate during impact as the difference between the initial kinetic energy E_{ki} and the residual kinetic energy E_{kf} [32] ($E_a = E_{ki} - E_{kf}$).

Commonly used for perforation tests, instrumented drop tests or instrumented pneumatic accelerators permit to obtain the evolution of the force on the striker and the striker displacement during perforation [12]. Image correlation techniques with high speed cameras, can also give the plate's straining during perforation [13]. The Hopkinson bar theory adapted for perforation are known for its high capacity of measure of the force during perforation [12,30].

During perforation of thin plates, petals appear. The number of cracks and their evolution during perforation are studied by various authors [9,23,27]. In particular, Atkins [2] determines the number of cracks using an analytical approach considering that the increment of total work of perforation is equal, during the transition from the step of plastic deformation, to the step of plastic deformation and crack propagation. But this approach is dependent on the initial radius of the crack front and so is difficult to apply.

Analytical models for perforation are already well established. One of the most used is Forrestal model [11] which is a hole growth based model. It which is known to be specially adapted for the perforation of thick plates. Forrestal deduced from the expression of the radial stress, the residual velocity and the ballistic limit velocity. More recently, Nazeer et al. [27] uses an energetic approach to determine the number of petals during perforation of thin plates. During the perforation, a conical nose striker induces bending deformation, stretching deformation and N cracks' propagation. Nazeer explains that the elastic bending work can be neglected. The sum of the bending plastic work W_b, the stretching plastic work W_s, the petals' bending work W_{bf} and the fracture work W_f is the total work of perforation W ($W = W_b + W_s + W_{bf} + W_f$). In a study of the petalling of plates during the perforation by a conical nose projectile, Wierzbicki [34] creates a bending energy and a tearing energy based model. Other analytical models can be quoted [3,10,24,35].

A numerical approach to model the perforation is also used by various authors. Finite element model (FEM) for thin plates

* Corresponding author.
E-mail address: leonard.antoinat@ensam.eu (L. Antoinat).

http://dx.doi.org/10.1016/j.ijimpeng.2014.07.017
0734-743X/.

perforations with a conical sticker was developed by various authors. Iqbal [17] used a Johnson–Cook behaviour law [20] and Johnson–Cook damage law for the material to model the perforation of a steel plate and an aluminium alloy plate. Borvik [6] used a modified Johnson–Cook behaviour law to simulate the perforation of an aluminium alloy plate. The results are in good agreement in term of velocity and in term of perforation type. Rodiguez-Martinez [32] used a modified Rusinek-Klepaczko model for the behaviour of a 2024-T3 aluminium alloy plate meshed with 3D brick elements. Dean et al. [9] used shell elements for the perforation of a steel plate and shows that it is well adapted for thin plates simulation. It can be noticed that for all of the authors, an isotropic behaviour for the plate's material is used.

Various numerical techniques are known to be well adapted for the study of dynamic crack propagation. The "kill elements" technique is the most popular and is used in FE software as Abaqus [1]. When the rupture criterion is reached in an element, the stress deviatoric part is taken as null or the element is deleted. To model a material rupture, a interface decohesive technique between two finite elements can be used. Introduced by Xu and Needleman [37]; the decohesion law characterises the behaviour of this area. This method is used for dynamic crack propagation for a well known crack travel [31]. The extended finite element method (X-FEM) has the advantage to simulate the free crack travel. During a mechanical solicitations involving rupture, the classical solution of elastic cracks' propagation [18] enriches the displacement field of the solution [29]. This method is used by Combescure et al. [8] for a study on a dynamic propagation of crack during a Zhou Rosakis Ravishandran's experiment (A projectile is launched on a pre-cracked sample). Others numerical methods exist to simulate crack propagation as phase fields model [14] or peridynamics [26].

During an impact, the material behaviour of the plate is affected by the local temperature variation induced by plastic strain [7]. Thus, the problem becomes thermomechanical. The coupling between the temperature and the strain is made with the help of a thermomechanical relation: $\rho c\dot{T} = \beta\sigma\dot{\varepsilon}^{p}$ where ρ is the density, c the thermal capacity, T the temperature, β the fraction of the rate of plastic work dissipated as heat, σ the stress and ε^{p} the plastic strain [15]. The β factor is considering as constant and equal to 0.9 in most of case, Clifton [7] shown that for an 2024-T3 aluminum alloy the β factor is plastic strain dependent. In a work on elastic crack propagation, Irwin [18] introduces the expression of crack tip stress and defined a stress intensity factor for each rupture mode (I, II, or III). This theory is the base of the rupture mechanic. Impact on ductile material involves high strain and so voids appear, grow, and coalesce until the rupture. Some rupture criterion exists to characterise this dynamic phenomenon. The Johnson Cook rupture model [21] and the Langseth model [5] are two rate dependent models used for perforation problems. Borvik et al. [5] uses the Langsteh model for the perforation of 12 mm thickness steel plates and Dean et al. [9] uses the Johnson–Cook model for the perforation of steel plates and predicted the formation of petals.

In this paper, a two-pronged approach for perforation is presented. Experimental tests on instrumented drop tests are made on 2 mm and 4 mm thickness 2024 T3 aluminium alloy plates. This alloy is known to have a rate dependent hardening behaviour. An example of tensile curve with a strain rate of 8000 s^{-1} is plotted in Fig. 1 [25]. An analytical model for perforation of thin plates based on energetic consideration is presented. The Forrestal approach is modified for the present case. It is concluded that it is limited for the perforation of thin plate of 2024 AA by a large diameter striker. During the perforation of thin plates of aluminium alloy, the evolution of the force is not a classic result of perforation. Three peaks of force can be observed. Each peaks will be explained with the help of a shell and a brick FE model. Numerical model, analytical model and experiments are compared and discussed with the help of the residual velocity, the absorbed energy and the impact force.

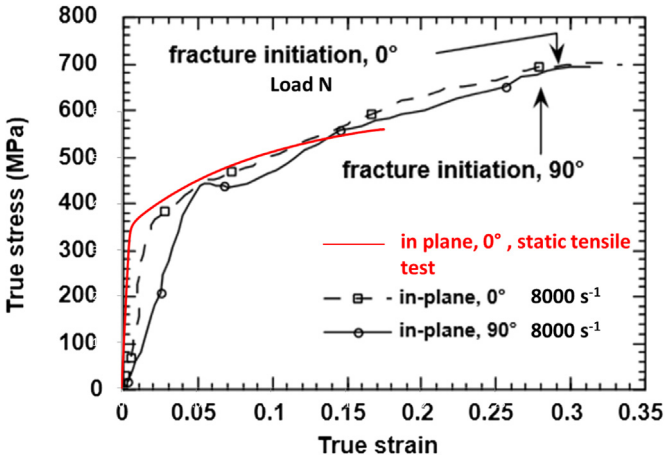

Fig. 1. Dynamic tensile test of 2024 AA 8000 s^{-1}) [25] compared to quasistatic tensile test on the studied 2 mm thick plate.

2. Experimental drop test on 2024 T3 aluminium alloy plates

A 2024-T3 aluminium alloy plate (2024-AA) (Al 4.76% *wt* Cu 1.38% *wt* Mg 0.65% *wt* Mn 0.22% *wt* Fe 0.08% *wt* Si 0.07% *wt* Zn 0.03% *wt* Ti 0.01% *wt* Cr) is perforated by a conical nose striker. Plates with a thickness of 2 and 4 mm are cut in squares of about 160 mm side length.

2.1. Experimental setup

With the help of an instrumented drop test (Fig. 2), a striker, with a 60° total angle conical nose and 45 mm diameter, perforates the plate. The striker is fixed on a trolley which slides on two bars from various heights and is associated with additional weight. A piezoelectric 9061A Kistler sensor allows the measurement of the force between the plate and the striker for a range of validity from 0 to 100 kN, with a relative error less than 5%. The trolley's displacement is measured by a Bullier laser sensor (error of 0.5%), with a 50 mm measure range. Those two sensors are completed with two high speed cameras. A Photron SA3 camera, (10 000 frames/s) is used to measure the striker displacement. Two mirrors enable the observation beneath the sheet by a Photron APX RS camera (9000 frames/s).The plate is fixed on a circular hole of 148 mm diameter with four screws where a 50 N m torque is applied.

Twenty three drop tests are performed, seventeen with 2 mm thick plates (tests 1–17) and six with 4 mm thick plates (tests 18–23). For the 2 mm thick plates, thirteen tests are made with a weight of the striker of 13 kg, two with a weight of 17 kg and two with a weight of 21 kg. A weight of 13 kg is used for the tests on 4 mm thick plates. Table 1 presents the tests.

2.2. Experimental results

2.2.1. Residual velocity

The velocity is calculated with the displacement measured with the laser sensor (Table 2). In order to filter the noise of high speed measurements, a moving average over 30 values of the velocity is calculated and a smoothed curve is obtained. If the moving average is taken over 10 or 50 values, the value of the residual velocity changes by ± 6% for 10 values and does not change for 50 values.

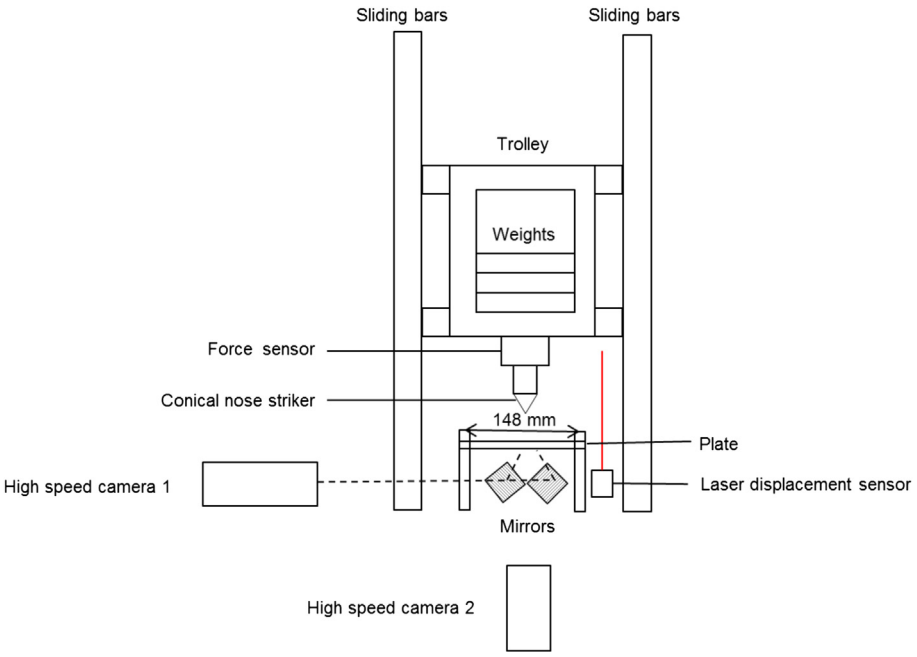

Fig. 2. Instrumented drop test.

The residual velocity of the striker for 2 mm plates after perforation is plotted as a function of the initial velocity (Fig. 3). If the plate is not completely perforated, the residual velocity is taken equal to 0. For an initial velocity greater than 5.5 m/s, there is complete perforation. The shape of the curve is a classical result of perforation tests [4,17,23]. For 4 mm thick plates, there is no complete perforation meaning that the ballistic limit velocity is greater than 6.3 m/s.

Table 1
Drop tests results (1–17: 2 mm thick plates, 18–23: 4 mm thick plates). The residual velocity is taken equal to zero if the plate is not totally perforated (- means "no petals").

Test number	Total mass (kg)	Height (m)	Initial velocity (m/s)	Initial kinetic energy (J)	Absorbed energy (J)	Petals number	Residual velocity (m/s)
1	13	0.4	2.8	51.0	40.0	4	0
2	13	0.4	2.8	51.0	40.0	4	0
3	13	1	4.1	62.5	47.8	5	0
4	13	1	4.2	66.6	51.9	5	0
5	13	1.5	4.8	149.8	138.8	6	0
6	13	1.5	4.8	149.8	140.4	4	0
7	13	1.8	5.9	196.6	152.7	6	2.6
8	13	1.8	5.9	203.8	163.2	5	2.5
9	13	2	6.1	241.9	166.7	4	3.4
10	13	2	6.1	241.9	187.2	4	2.9
11	13	2.1	6.4	267.5	178.6	5	3.7
12	13	2.3	6.7	293.0	199.2	5	3.8
13	13	2.5	6.9	309.5	171.9	6	4.6
14	17	1.3	5.0	212.5	178.5	5	2
15	17	1.3	5	212.5	185.0	5	1.8
16	21	1	4.4	203.3	190.6	5	1.1
17	21	1	4.4	203.3	192.8	5	1
18	13	0.4	2.8	51.0	22.3	–	0
19	13	0.4	2.8	51.0	13.5	–	0
20	13	0.8	4.0	104.0	66.6	–	0
21	13	1.2	4.8	149.8	102.4	–	0
22	13	1.6	5.6	203.8	152.9	–	0
23	13	2	6.3	258.0	210.6	–	0

2.2.2. Force results

For each test, the force is plotted as a function of time (Figs. 4 and 5). Analysis of results show a good repeatability.

For the 2 mm thick plates' perforation, a first peak of force from 0.5 kN to 1.5 kN is observed on Fig. 3 (a–f). After the force begins to rise until the first crack appearance. A minor fall of the force is observed (peak 2) and corresponds to the beginning of the crack propagation. When the crack is long enough, the force starts to increase sparsely until a third peak force i.e. when the perforation is completed. The force is also plotted as a function of the striker displacement (Fig. 6). For the studied velocity range (0–6.7 m/s), levels of force are similar for a same displacement. The first and the second peaks of force are observed in all tests. After the second peak force, the force rises in the same way and until a value depending of the initial velocity. If the plate is totally perforated, the same force is reached for the second peak. The area under the

Table 2
Notations for the analytical models of perforation.

σ_y	Yield stress
R_0	Radius of the plate
t_0	Thickness of the plate
ϕ	Half angle of the striker
r_0	Radius of the striker
ν	Poisson's ratio
G	Fracture toughness
E	Young modulus
ρ_p	Density of the plate
B_0 , σ_s	Specific material parameters of the Forrestal model
F	Force of impact
m	Mass of the striker
A	Area of contact between the striker and the plate
W_e	Elastic work
W_b	Bending plastic work
W_s	Stretching plastic work
W_{bf}	Petals' bending work
W_f	Fracture work
z	Displacement of the striker
z_b	Ultimate bending displacement before rupture
L	Length of fracture
β	Bending angle of the plate

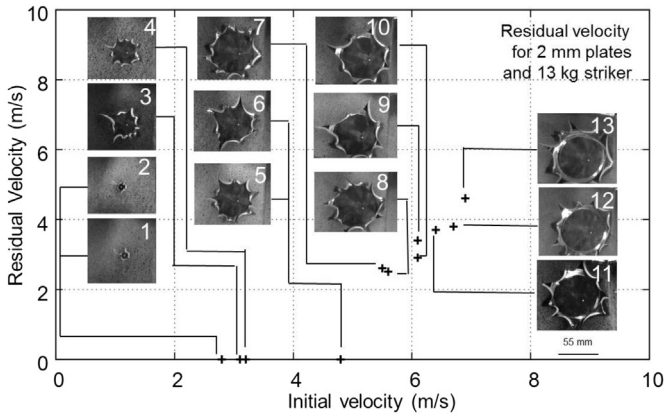

Fig. 3. Residual velocity as a function of initial velocity for a 13 kg striker and 2 mm thick plates.

force vs displacement curve represents the energy absorbed during perforation. Thus, it can be deduced that the energy needed to perforate the plate is constant. Numerical simulations will permit a better analysis of the force evolution and a better understanding of the observed peaks.

For the 4 mm thick plates perforation, a rise of the force as a function of the time is observed until a maximum corresponding to the rebound of the striker (Fig. 5a–e). A similar force fo a same displacement is observed for all tests (Fig. 5f).

2.2.3. Crack and petals' observation

When the force reaches the second peak, cracks and petals appear. The number of cracks is always greater than 4 (Table 2). Some other cracks can appear during perforation. No conclusion can be made on this number of petals. The crack propagation takes about 10 ms. The mean crack velocity can be measured with the use of high speed camera pictures. According to Fig. 7, this velocity increases linearly with the initial velocity and lies between 1 m/s and 3.5 m/s. This velocity is half the value of the initial velocity corresponding to the radial velocity of the striker ($V_r = tan(\phi)V$, $\phi = 30°$). The value of the slope seems to be equal to $tan(\phi)$. This must be confirmed with other striker's angle. When a crack appears, its velocity rapidly rises to a maximum and then falls until the end of the perforation. This peak of velocity occurs when the first peak force is falling. Numerical simulations will permit a better analysis of the crack propagation.

Atkins [2] determines the number of petals with an energetic approach and considering that an initial radius of perforation r_p is well known before the start of crack propagation:

$$n = \frac{2\pi\sigma_y r_p \varepsilon_f}{G} \quad (1)$$

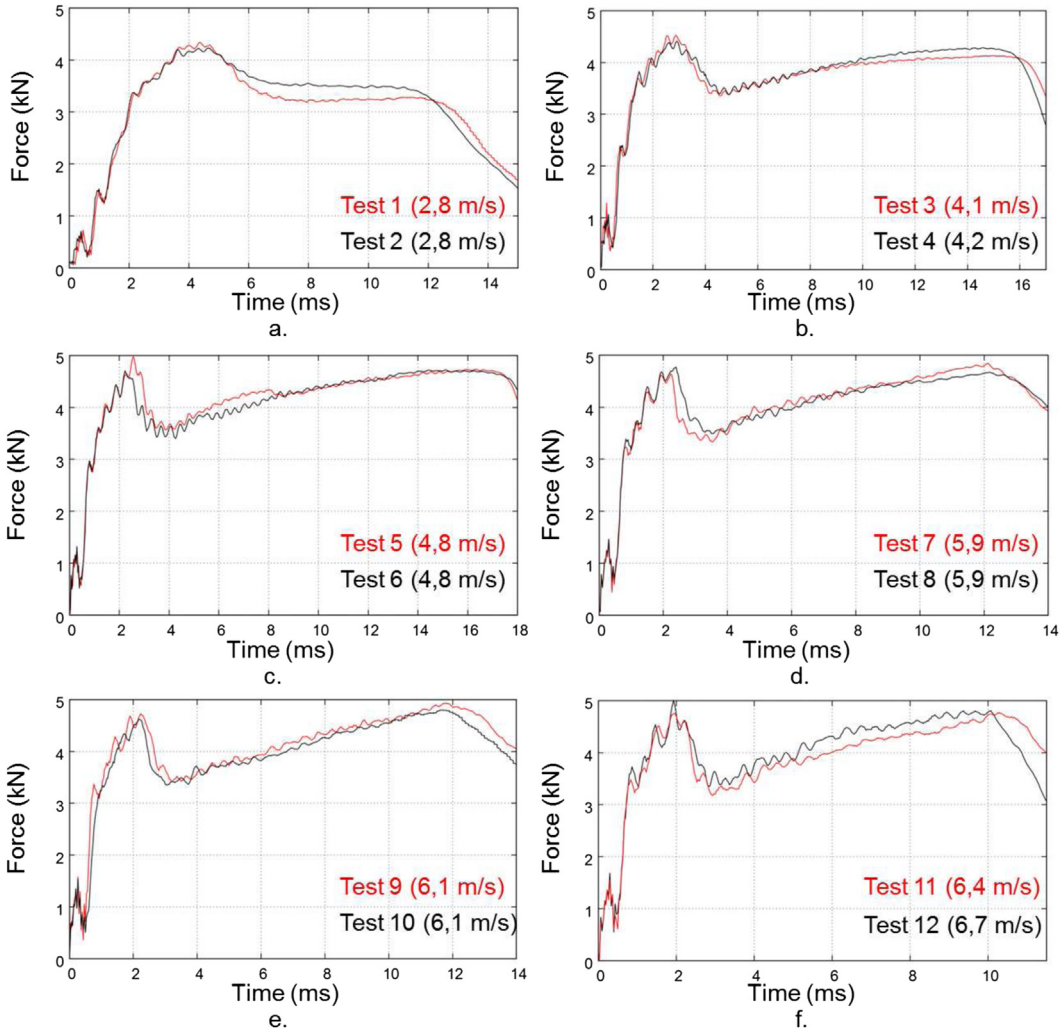

Fig. 4. Force as a function of time for 2 mm thick plates.

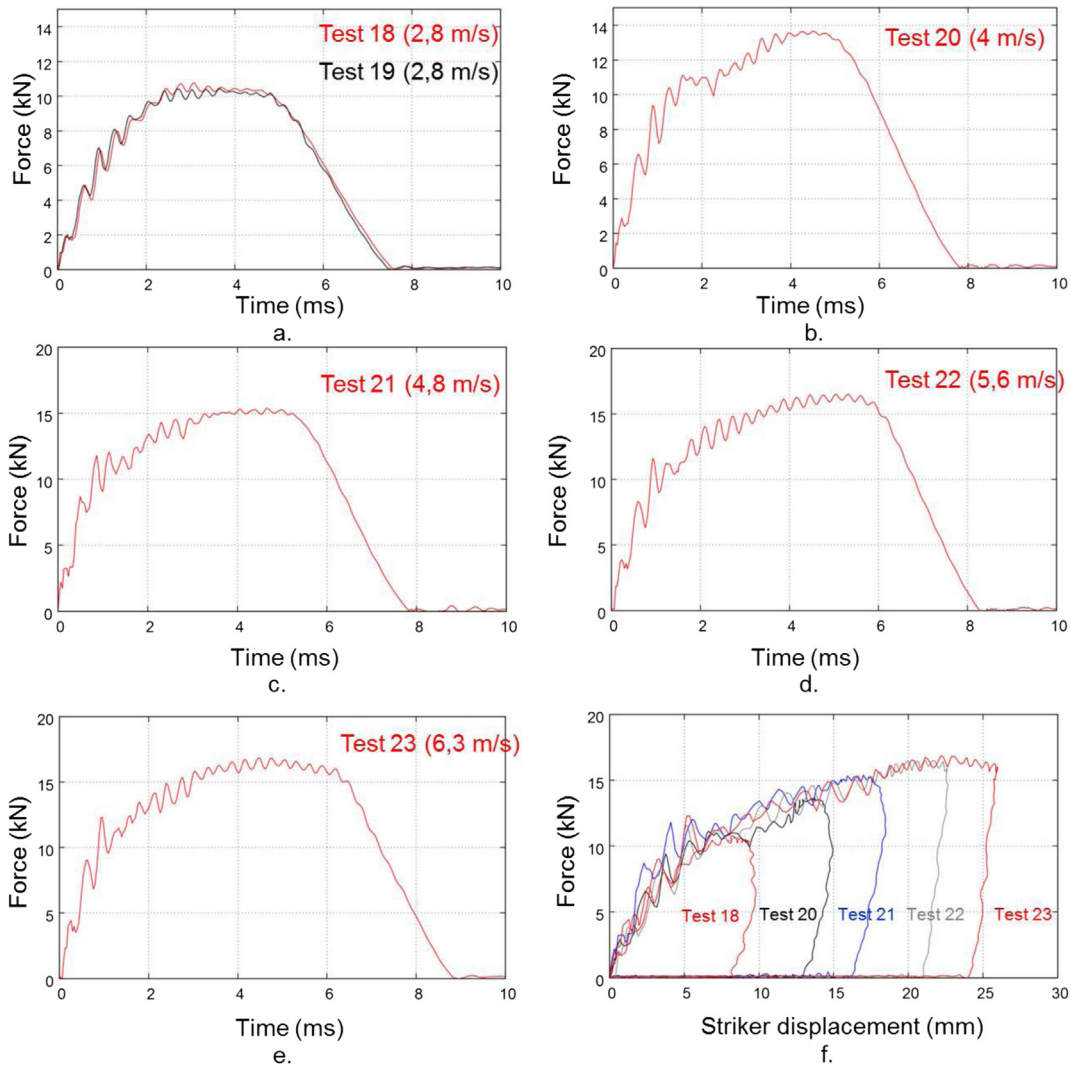

Fig. 5. Force as a function of time and displacement of the striker for 4 mm thick plates.

where σ_y is the yield stress, ε_f is the fracture strain and G is the fracture toughness. Atkins suggests an evolution of the equation (1) to determine the number of petals when there is no starter hole ($r_p = 0$). He considers that the initial radius can be estimate as $r_p = 1/2t_0 tan(\phi)$ (t_0 is the thickness of the plate and ϕ is the semi angle of the striker). Thus the Equation (1) becomes:

$$n = \frac{\pi\sigma_y \tan(\phi) t_0 \varepsilon_f}{G} \tag{2}$$

In Fig. 1, a quasistatic tensile test performed in this study for 2 mm thick plate ($\dot{\varepsilon} = 10^{-3}s^{-1}$) is compared to literature results by

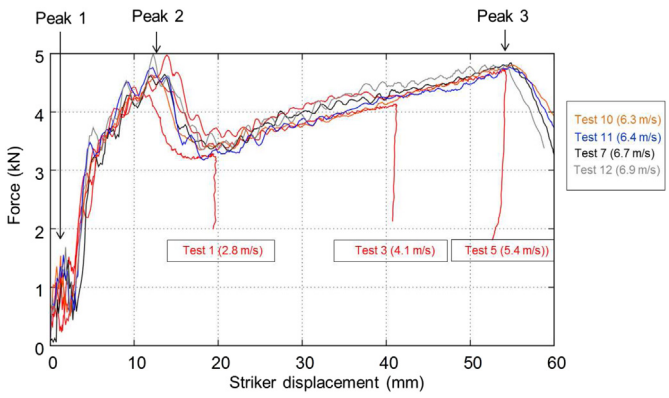

Fig. 6. Force as a function of displacement of the striker for 2 mm thick plates.

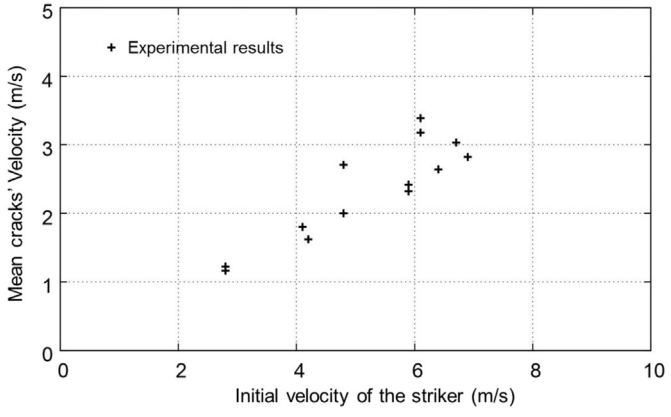

Fig. 7. Mean cracks' velocity as a function of initial velocity of the striker for 2 mm thick plates.

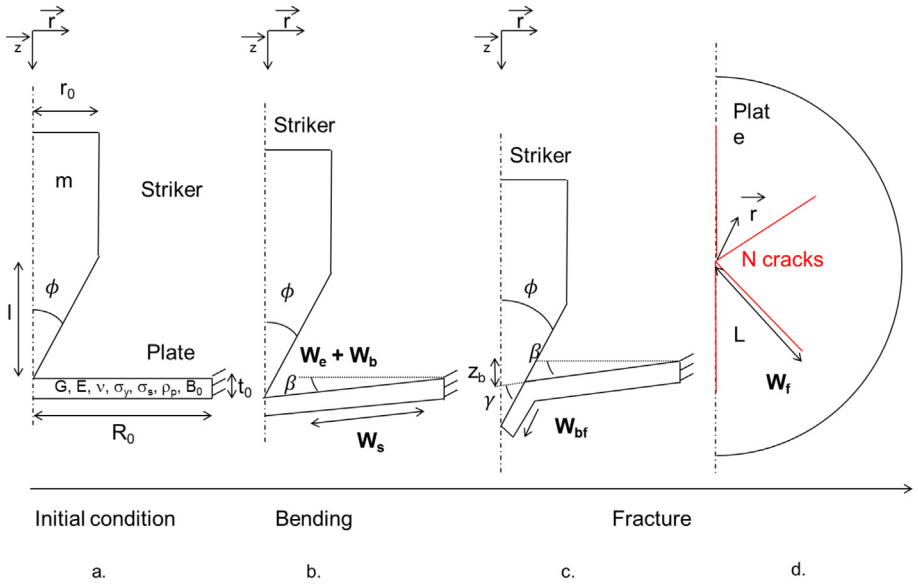

Fig. 8. Analytical model for perforation [27].

Lesuer [25]. Whereas Lesuer gives a fracture strain of 0.3 at 8000 s^{-1}, the presented results on the studied plate give a fracture strain of 0.18. Thus the number of petals is equal to 2 in a static case and 3 for a dynamic case ($\sigma_y = 369\ MPa$, $t_0 = 0.002\ mm$, $G = 116600\ J/m^2$). Results are not in the range of experimental data (4–6 petals). The initial radius of perforation is now changed to the radius of the hole when the striker appears on the distal side of the plate $r_p = t_0 tan(\phi)$. Thus, the number of petals is 4 ($\varepsilon_f = 0.18$) and 6 ($\varepsilon_f = 0.3$) and results are close to experimental ones (Table 2).

3. Models for perforation

Two models for perforation are presented. In section 3.1, the model is an analytical one. In section 3.2, a shell finite element model is used.

3.1. Analytical model for perforation

Analytical methods can also be used to determine the ballistic limit velocity. A conical nose striker of mass m with an angle 2ϕ, a radius r_0 and a length of conical part l impacts a plate of radius R_0 and thickness t_0 as shown in Fig. 8. The yield stress of the plate is σ_y, the toughness G, the Young modulus E, the density ρ_p and the Poisson's ratio ν. One of the most used analytical model is the Forrestal's model [11] which is a hole growth based model and which is known to be specially adapted for the perforation of thick plates. A good approximation for the behaviour of the material during perforation is to consider that the radial stress in the plate can be expressed as a function of the hole expansion velocity V as $\sigma = \sigma_s + \rho_p B_0 V^2$. Specific material parameters of the Forrestal model are σ_s and B_0 (Fig. 9a).

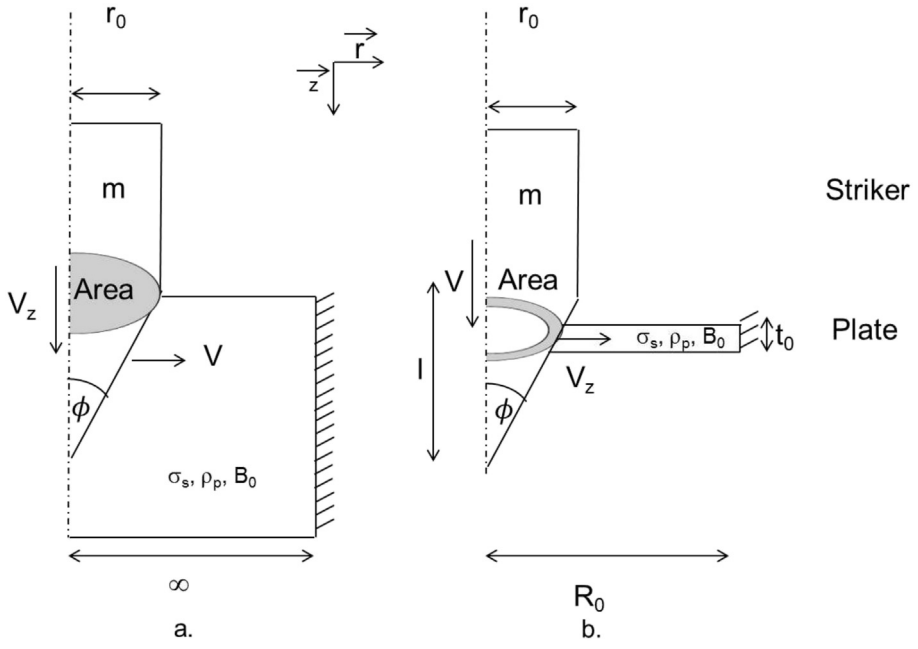

Fig. 9. Forrestal model for perforation (a) and modified Forrestal model for thin plates (b).

Table 3
Parameters of the analytical model.

σ_y (MPa)	G (J/m^2)	E (GPa)	R_0 (mm)	r_0 (mm)	t_0 (mm)	z_b (mm)	ϕ (°)	N
369	116 600	70	74	22.5	2 & 4	4(2 mm) 5(4 mm)	30	4, 5, 6

The axial force F_z in the plate can be written as $F_z = A\sigma = A(\sigma_s+\rho_p B_0(V_z tan(\phi))^2)$ where A is the area of contact between the striker and the plate and $V = V_z tan(\phi)$ the radial velocity (V_z is the axial striker velocity).

This approach for perforation is modified for the perforation of thin plates. According to the equilibrium applied on the striker, and because the friction force is neglected, it is possible to write.

$$m\frac{dV_z}{dt} = mV_z\frac{dV_z}{dz} = -F_z = -A(\sigma_s + \rho_p B_0(V_z^2 tan^2(\phi)) \quad (3)$$

and so:

$$\frac{dV_z^2}{1+aV_z^2} = bAdz \quad (4)$$

with: $a = \rho_p B_0 tan^2(\phi)/\sigma_s$ and $b = 2\sigma_s/m$

Since the first penetration of the striker in the plate, ie until the perforation equals the thickness of the plate and the end of the perforation are neglected, only the part of the conical nose in contact with all the thickness of the plate is considered. Forrestal considers that the area A equals to the area of the cylindrical part of the striker (Fig. 9b). In the case of thin plates, this area is smaller because a part of the conical nose perforates the plate. This area is expressed as $A = \pi(z^2 tan^2(\phi) - (z - t_0)^2 tan^2(\phi))$. With an integration of equation (2) from $z = 0$ to $z = l$ and from Ref. $V_z = V_{bl}$ (the ballistic limit velocity) to $V_z = 0$, the ballistic limit velocity can be deduced as:

$$\frac{1}{a}\ln\left(1 + aV_{bl}^2\right) = \pi\left(l^2 t_0 - lt_0^2\right)tan^2(\phi)b \quad (5)$$

$$V_{bl} = \sqrt{\frac{1}{a}\left(\exp(\pi(l^2 t_0 - lt_0^2)tan^2(\phi)ba) - 1\right)} \quad (6)$$

For an aluminium alloy 2024 T3, σ_s and B_0 have been identified on quasistatic tensile tests such as $\sigma_s = 1460$ *MPa* and $B_0 = 3.4$ following the procedure proposed by Forrestal et al. [11]. The ballistic limit velocity is calculated as equal to 27 m/s. This value of ballistic limit velocity is higher than the measured velocity. Thus the Forrestal model is not adapted for the perforation of thin plates.

An energetic approach for perforation [27] is modified to find the residual velocity of the striker during perforation. The

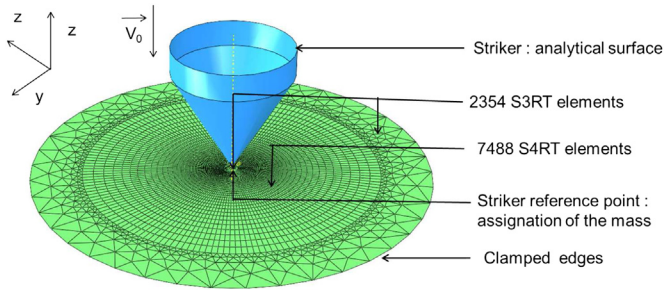

Fig. 10. Finite element shell model.

Table 4
Johnson Cook law parameters for equation (14).

A (MPa)	B (MPa)	n	C	m	T_{melt} (K)	T_{room} (K)	$\dot{\varepsilon^p}$
369	684	0.73	0.0083	1.7	775	293	1

perforation work is the sum of the bending elastic work W_e, the bending plastic work W_b, (Fig. 8b) the stretching plastic work W_s (Fig. 8c), the petals' bending work W_{bf}, and the fracture work W_f (Fig. 8d) and can be taken equal to the absorbed energy. The different contributions to the total energy are explained in subsections 3.1.1 to 3.1.5. Thermal and friction works are neglected. The residual velocity V_r is expressed as a function of the initial velocity V_0 and the striker mass m such as:

$$V_r = \sqrt{V_0^2 - \frac{2\left(W_e + W_b + W_s + W_{bf} + W_f\right)}{m}} \quad (7)$$

The ballistic limit velocity V_{bl} is a particular case of equation (5) when $V_r = 0$ m/s and is given by:

$$V_{bl} = \sqrt{\frac{2\left(W_e + W_e + W_s + W_{bf} + W_f\right)}{m}} \quad (8)$$

3.1.1. Bending elastic work W_e

When the plate is in contact with the striker, elastic deformation occurs in the plate until plastic behaviour (ie when the radial stress σ_r equals the yield stress). The elastic work W_e can be expressed with the help of the elastic bending of circular plates theory where the plate is clamped on the edges with a concentrated center force F [36]. Since the thin plate theory gives an infinite value of the central bending moments, an empirical approximation (for steel, but acceptable for aluminium and copper alloys) of the force of elastic bending F in function of the displacement z is given by Xiong [36]:

$$F = \frac{zEt_0^3}{0.217R_0^2} \quad (9)$$

The elastic work is the integration of the force along the displacement and can be expressed from equation (8) as:

$$W_e = \int_0^{z_b} Fdz = \frac{z_b^2 Et_0^3}{0.434R_0^2} \quad (10)$$

Where z_b is the ultimate bending displacement before rupture.

3.1.2. Bending plastic work W_b

Considering that the material has a perfectly plastic behaviour and that a plastic hinge occurs at radius R_0, the plastic bending work W_b is written as:

$$W_b = \pi\sigma_y t_0^2 R_0 \beta \quad (11)$$

Where the bending angle is β (calculated as a function R_0 and the striker displacement z as $tan(\beta) = z/R_0$ (Fig. 8)).

Table 5
Damage Johnson Cook law parameters for equation (15).

D_1	D_2	D_3	D_4	D_5	$\dot{\varepsilon_{0^{pf}}}$
0.13	0.13	−1.5	0.011	0	1

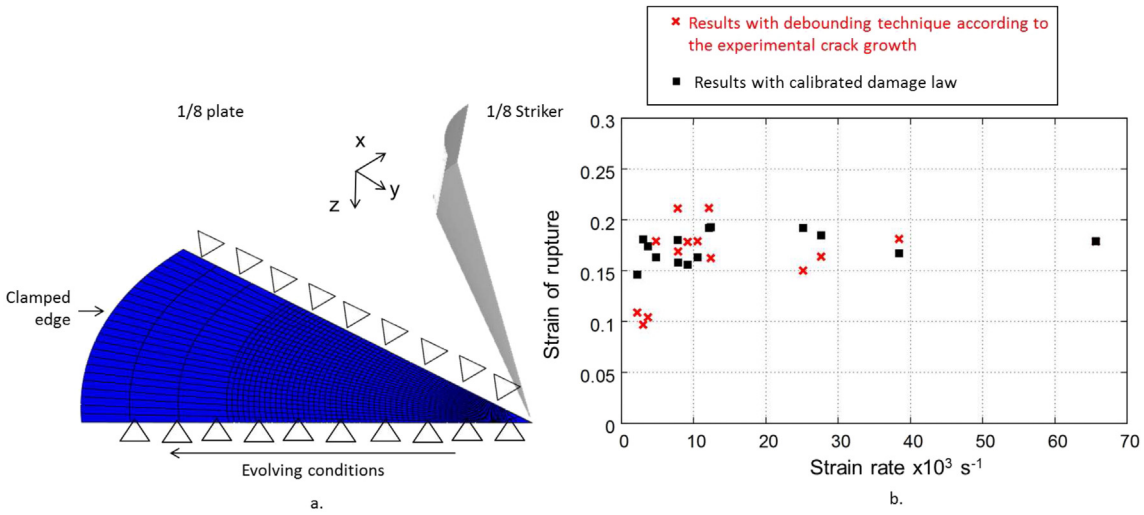

Fig. 11. FE model of eighth of plate (a) and strain of rupture as a function of strain rate to calibrate the damage JC law (b).

3.1.3. Stretching plastic work W_s

During the bending, the plate is stretched, and so its thickness is reduced. The stretching work Ws is the result of this effect and is expressed as:

$$W_s = (\pi R_0)^2 \sigma_y t_0 \varepsilon_s \tag{12}$$

where ε_s is the stretching strain, defined thanks to the evolving surface area of the sheet and its original area ($\varepsilon_s = \ln(\sqrt{R_0^2 + z^2}/R_0)$.

3.1.4. Petals' bending work W_{bf}

When the first crack is appearing, petals are forming in the plate. These petals bend, until the striker passes through the plate. The petals' bending work can be written as [27]:

$$W_{bf} = \pi \sigma_y r_0 t^2 \frac{\gamma}{2} \frac{2+N}{1+N} \tag{13}$$

where N is the number of petals and γ is the angle made by petals and equals to $\pi/2 - \beta - \phi$.

3.1.5. Fracture work W_f

The fracture work due to crack propagation is the sum of the work involved by each crack and can be expressed as a function of the fracture toughness G, the thickness t and the length of fracture L by Ref. $W_f = NGtL$. The thickness t can be expressed as $t = t_0/\sqrt{1 + z_b^2/R_0^2}$ where z_b is the ultimate bending displacement at the onset of cracking [27]. L is taken equal to the projection of the striker's radius on the bending sheet ($L = \sqrt{r_0^2 + z_b^2}$). Thus the fracture work is given by:

$$W_f = NGt_0 \Big/ \sqrt{1 + z_b^2/R_0^2}\sqrt{r_0^2 + z_b^2} \tag{14}$$

3.1.6. Constants for the analytical model

The model depends on the number of cracks and the ultimate bending displacement z_b. Parameters of the model are given in Table 3. Material properties E, σ_y are obtained from tensile test and the nonlinear fracture toughness G is taken from Jones et al. [22]. The displacement z_b has been measured on the plates and equals

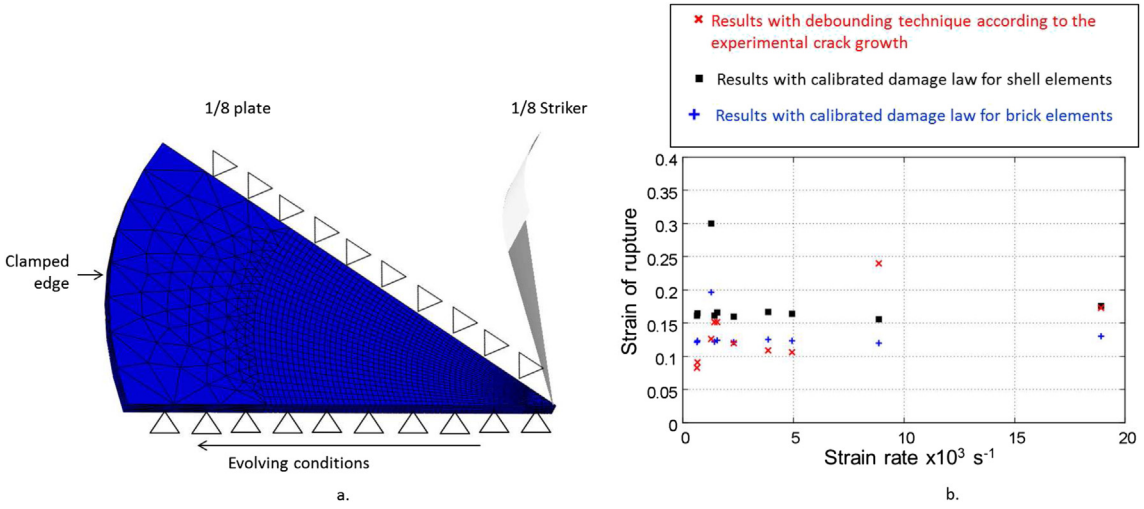

Fig. 12. FE brick model of eighth of plate (a) and strain of rupture as a function of strain rate to calibrate the damage JC law (b).

4 mm and 5 mm respectively for 2 mm and 4 mm thick plates. The elastic bending work W_e can be neglected compared to other works ($W_e = 0.26\ J$ $W_b = 18.5\ J$ $W_s = 58.2\ J$ $W_{bf} = 62.0\ J$ $W_f = 21.3\ J$ for $t_0 = 2\ mm$).

3.2. Finite element model for perforation

A three-dimensional shell finite element model is developed in Abaqus/Explicit to simulate the perforation of 2024-AA plates. The deformation of the striker during impact is neglected and so it can be modelled as an analytical rigid surface with an associated mass reference point. The behaviour of the material is modelled by a Johnson–Cook law for deformation and fracture described in section 3.2.1. 2024-AA plates are meshed with 19842 shell elements type (S). The plate is divided in three parts (Fig. 10), the center of plate with triangle type elements S3RT, the second part with 7488 reduced quadrangle type elements S4RT and the transition part with triangle type elements S3RT. The total number of S3RT element is 2354. Five integration points are chosen in the thickness (2 mm and 4 mm) of each shell elements for stability reasons. The penality contact between the plate and the striker is used with no friction. Temperature effects are taken into account. Initial velocities of simulations are taken similar to experimental drop tests. Other simulations with an initial velocity of 8 m/s are performed for 2 mm thick plates and 10 m/s, 12 m/s and 15 m/s for 4 mm thick plates. To conclude, the shell model and the brick model give similar result.

3.2.1. 2024 T3 AA behaviour law

The Johnson–Cook (JC) behaviour law [20] is applied to the material:

$$\sigma = (A + B\varepsilon^{pn})\left(1 + C\ln\left(\frac{\dot{\varepsilon}^p}{\dot{\varepsilon}_0}\right)\right)\left(1 - \left(\frac{T - T_{room}}{T_{melt} - T_{room}}\right)^m\right) \quad (15)$$

where A, B, n, C, m, the reference strain rate $\dot{\varepsilon}_0$ and the melting temperature T_{melt} are material parameters, T is the test temperature, T_{room} is the room temperature and $\dot{\varepsilon}^p$ is the plastic strain rate.

Because of the high strain rate involved in the material during perforation, a strain rate fracture model must be used. The Johnson–Cook model for the fracture [21] is chosen given the fracture strain as:

$$\varepsilon_f = \left(D_1 + D_2 e^{D_3 \frac{p}{\sigma_{eq}}}\right)\left(1 + D_4 \ln\left(\frac{\dot{\varepsilon}^p}{\dot{\varepsilon}^p_{0f}}\right)\right)\left(1 - D_5\left(\frac{T - T_{room}}{T_{melt} - T_{room}}\right)\right) \quad (16)$$

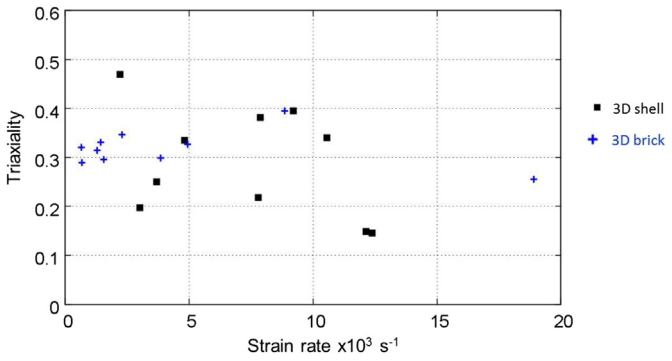

Fig. 13. Triaxiality in function of strain rate for debonding models.

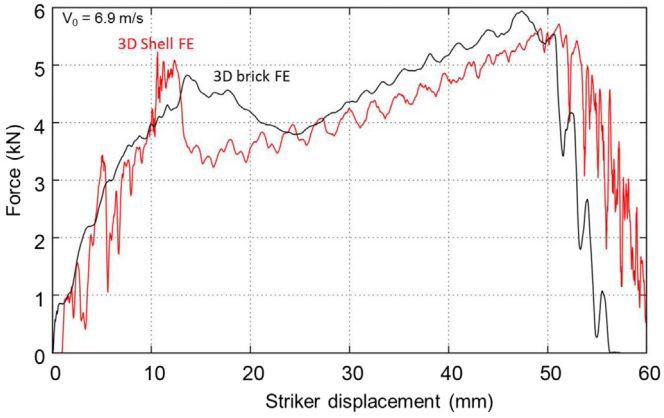

Fig. 14. Force in function of striker displacement for the 3D shell model and the 3D brick model.

where D_1, D_2, D_3, D_4, D_5, T_{melt}, $\dot{\varepsilon}_{0Pf}$ are material parameters, p is the hydrostatic pressure, σ_{eq} the Mises stress, T is the test temperature and T_{room} is the room temperature.

The elastic behaviour is considered as isotropic. The Young modulus E equals 70 GPa, the Poisson's ratio ν equals 0.3. All parameters are taken from the literature [25] and resumed in Table 4 and Table 5. Lesuer identifies JC parameters with Hopkinson pressure bar tests until a strain rate of 8000 s^{-1}. Because of high strain rate a thermomechanical coupling is used. The β factor is considered as constant and equal to 0.9. The thermal capacity equals to 897 J/kg/K and the thermal conductivity equals to 237 W/m/K.

3.2.2. Enhancement of the calibration of the damage Johnson Cook law

Damage JC law parameters given by Lesuer [25] are not well suited to model the behaviour of the 2024-AA during perforation (bad results in terms of force level). In order to enhance the calibration of the JC damage law, a 3D shell FE model considering on eighth of a 2 mm thick plate is used as shown in Fig. 11(a). The initial velocity is taken equal to 6.4 m/s (drop test number 11). The main objective is to study the crack phenomenon influence on the perforation force considering that only four cracks appear during perforation. Thus, the true crack velocity, obtained from experimental results of the high speed camera, is imposed on an edge of the model using a debonding technique (Fig. 11a). This debonding technique will permit to obtain the maximal strain before fracture according to strain rates and the maximal stress at the crack tip. The strain of fracture is plotted as a function of strain rate in Fig. 11(b) and will be compared with the JC law model. The strain of fracture seems to be highly strain rate dependent.The calibration of the damage JC law parameters is enhanced to fit the curve. The

Table 6
FE Simulations results for 2 mm thick plates.

Test number	Total mass (kg)	Initial velocity (m/s)	Absorbed energy (J)	Petals number	Residual velocity (m/s)
1	13	2.8	46.8	4	0
2	13	4.1	101.4	5	0
3	13	4.8	140.4	5	0
4	13	5.9	207.5	5	1.7
5	13	6.1	207.5	5	2.3
6	13	6.4	207.7	5	3
7	13	6.7	216.6	5	3.4
8	13	6.9	229.5	4	3.5
9	13	8.0	226.46	4	5.4

Table 7
FE Simulations results for 4 mm thick plates.

Test number	Total mass (kg)	Initial velocity (m/s)	Absorbed energy (J)	Residual velocity (m/s)
10	13	2.8	39.9	0
11	13	4	91.3	0
12	13	4.8	135.1	0
13	13	5.6	187.2	0
14	13	6.3	239.2	0
15	13	10	606.1	0
16	13	12	798.5	4.6
17	13	15	759.5	10.4

parameter D1 has thus been modified to 0.07. New JC damage parameters will be used for simulations with 3D shell model.

3.2.3. Comparison with a 3D brick finite element model for perforation

The three-dimensional shell finite element model is compared with a three-dimensional brick finite element model for the perforation of a 2 mm thick plate and an initial velocity of 6.9 m/s with the same conditions. The plate is meshed with 35280 reduce brick C3D8RT elements and with 13317 tetrahedral C3D4T elements (5 elements in the thickness). The contact between the striker and the plate is taken as perfect. In concern of the rupture behaviour, the value of the D_2 parameter is adjusted to 0.07 according to the same previous calibration technique involving debonding with 3d brick elements (Fig. 12). The mean fracture strain ahead of the crack tip is around 0.12 (Fig. 12b) and is less than the fracture strain found with shell elements. The calibration of the D_2 parameter affects the effect of the stress triaxiality. For each debonding model (shell and brick), the calculated triaxiality is plotted in function of the strain rate in Fig. 13. With the brick approach, the triaxiality ahead of the crack tip is around 0.3 and higher than the triaxiality calculated with shell elements. The 3D shell and brick models with their respective failure parameters are applied to the simulations of the perforation of a complete plate and are compared in term of force vs displacement in Fig. 14. The number of petals is equal to 6 in the brick model (4 for the shell model). In the two models, the residual velocity is equal to 3.5 m/s.

Although the 3D brick model could be considered as more realistic for the perforation since it permits to capture out-of plane stress effects and the in-depth crack propagation, comparing CPU times, the 3D brick model is 14 times longer than the shell model. The advantage of the shell model is also that it leads to fewer problems of finite elements' distortions.

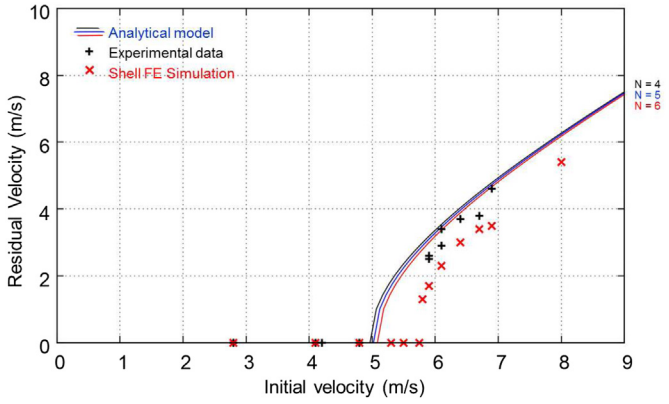

Fig. 15. Residual velocity as a function of initial velocity for a 13 kg striker and 2 mm thick plates for experiments, FE simulation and analytical model (*N* is the number of petals).

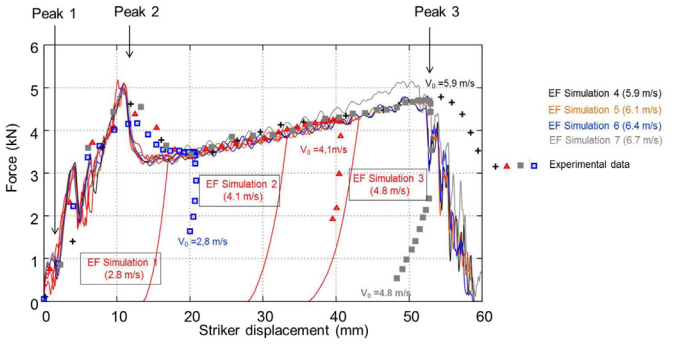

Fig. 16. Simulated force as a function of displacement of the striker for 2 mm thick plates.

4. Results and discussions

Results of the FE simulations in terms of absorbed energy, petals number and residual velocity are resumed in Table 6 and Table 7 respectively for 2 mm and 4 mm thick plates. When applicable, results are compared to the analytical model.

4.1. Striker velocity and perforation force

The residual velocity is plotted, for each test with a mass of 13 kg and a 2 mm thick plates, as a function of initial velocity in Fig. 15. The analytical model is plotted for a number of petals equals to 4, 5 and 6. It predicts a good range of residual velocity. The shell FE model tends to underestimate residual velocities measured during drop tests. The ballistic limit velocity is respectively 5.0 m/s, 5.0 m/s and 5.1 mm for 4, 5 or 6 petals for the analytical model. Other simulations are performed with an initial velocity between 5 m/s and 6 m/s. From 5 m/s to 5.75 m/s, the perforation is not completed. For 5.8 m/s the residual velocity is 1.3 m/s. Thus, the ballistic limit velocity is around 5.8 m/s.

For the configuration of a 3 m drop test - 4 mm thick plates, the ballistic limit velocity cannot be reached in the experiment. However, numerical and analytical models will permit to approximate the value of the ballistic limit velocity and the energy needed for perforation. For a number of petals of 4, 5 and 6 the ballistic limit velocity predicted by the analytical model is respectively of 9.2 m/s, 9.3 m/s and 9.4 m/s (absorbed energy is between 562 J and 572 J). According to the simulation the absorbed energy needed to perforate the plate is around 760 J – 800 J. The ballistic limit can be evaluated around 11 m/s. As for 2 mm thick plates, the simulated ballistic limit velocity is higher than the analytic velocity.

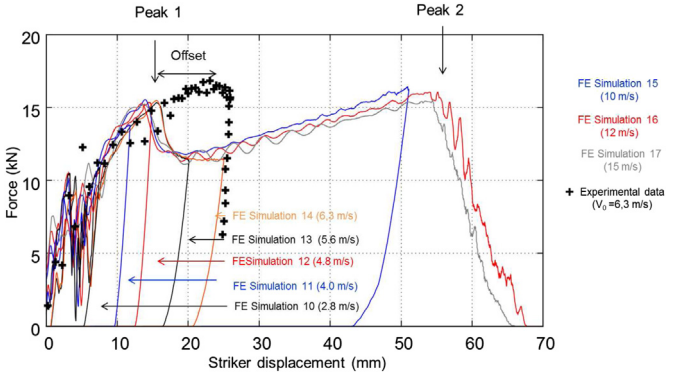

Fig. 17. Force as a function of displacement for 3D Shell FE simulations (4 mm thick plate).

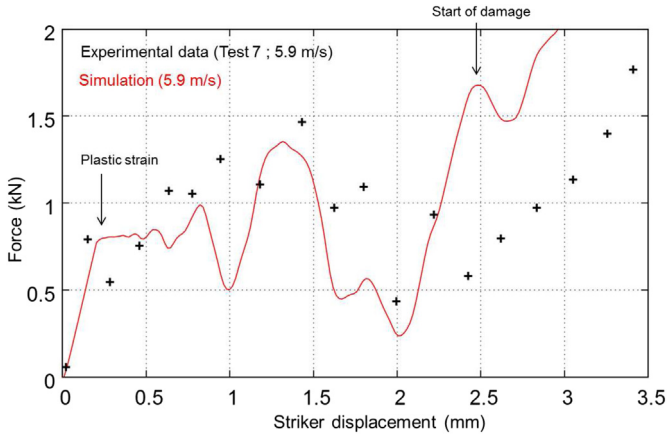

Fig. 18. First peak force as a function of the time for a 13 kg striker and 2 mm thick plates (test 9).

Experimental and calculated forces are compared for 2 mm thick plates. Simulated impact forces are plotted as a function of displacement in Fig. 16. Three peaks of force can be observed. For simulation 1, 2 and 3, there is a no complete perforation. For an initial velocity higher than 5.9 m/s the plate is perforated. Each peak force will be discussed and explained in section 4.2. The experimental force is also plotted for an initial velocity of 2.8 m/s, 4.1 m/s, 4.8 m/s and 5.9 m/s. For low initial velocities, the maximal displacement of the striker is higher for the experiment than the simulation. This difference rises with the initial velocity. Thus, the numerical model gives good results in term of force level, but the maximal displacement before the rebound is not perfectly predicted.

The force during perforation is plotted as a function of the displacement of the striker for each simulations in Fig. 17 for 4 mm thick plates. As in experiments, the force is similar at a same displacement. The simulations present a peak force that is not easily observed in experiments on 4 mm thick plates unlike experiments on 2 mm thick plates.

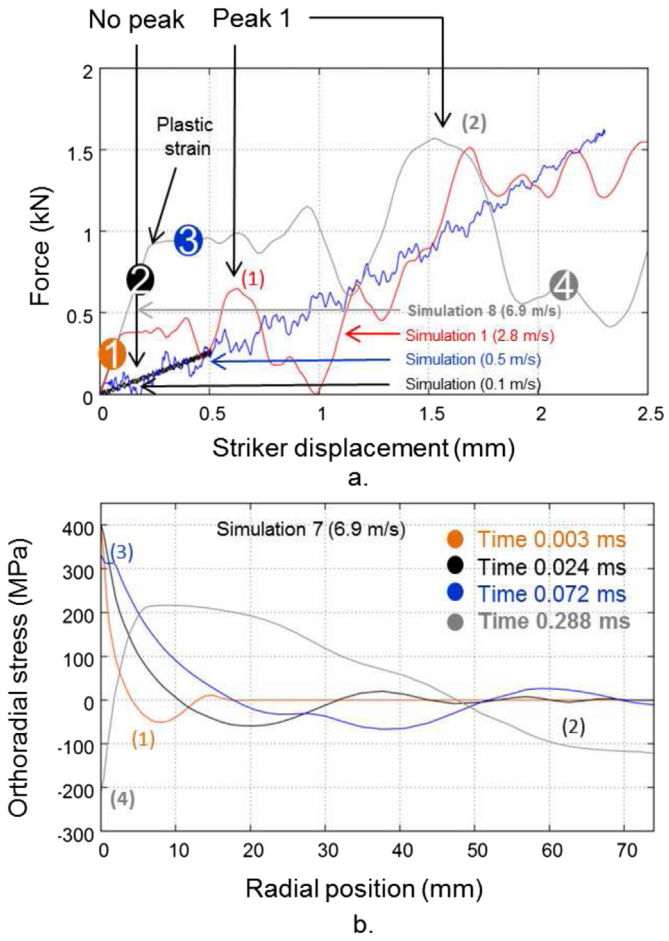

Fig. 19. First peak force as a function displacement for four initial velocities (0.1 m/s, 0.5 m/s, 2.6 m/s and 6.9 m/s) (a) and shock wave propagation in the plate (b). (For interpretation of the references to colour in this figure legend, the reader is referred to the web version of this article.)

4.2. Analysis of peak forces for 2 mm thick plates

The first peak force, simulated during impact by the shell FE model, remains difficult to analyse. The experimental and the simulated first peak are plotted for an initial velocity of 6.1 m/s in Fig. 18. The simulated force rises and then oscillates around a value. The maximal value of the peak force is similar for the simulation and the experiment. The first peak explained by the shock wave propagation since no failure is predicted by the model at this time. In Fig. 19(a), the first peak is plotted as function of the striker displacement in the case of four initial velocity (0.1 m/s, 0.5 m/s, 2.8 m/s, 6.9 m/s). The maximal value of the peak decreases when the initial velocity falls. In the figure, it passes from 1.5 kN (point 2) for the velocity of 6.9 m/s to 0.6 kN (point 1) for an initial velocity of 2.8 m/s. When the initial velocity is low (i.e. 0.1 m/s and 0.5 m/s), the first peak force disappears.

The striker deforms the plate and involves shock wave propagation. This shock wave in terms of the orthoradial stress is plotted in Fig. 19(b) as function of radius of the plate, for various times after impact, before and after the first peak. After impact, the force rises (Fig. 19a orange point) and the shock waves starts to propagate from the center to the edge (Fig. 19b. (1)). Because of the clamped condition, the wave is reflected (Fig. 19b. (2)) and the force continues to rise (Fig. 19a black point). The Yield stress is reached in the

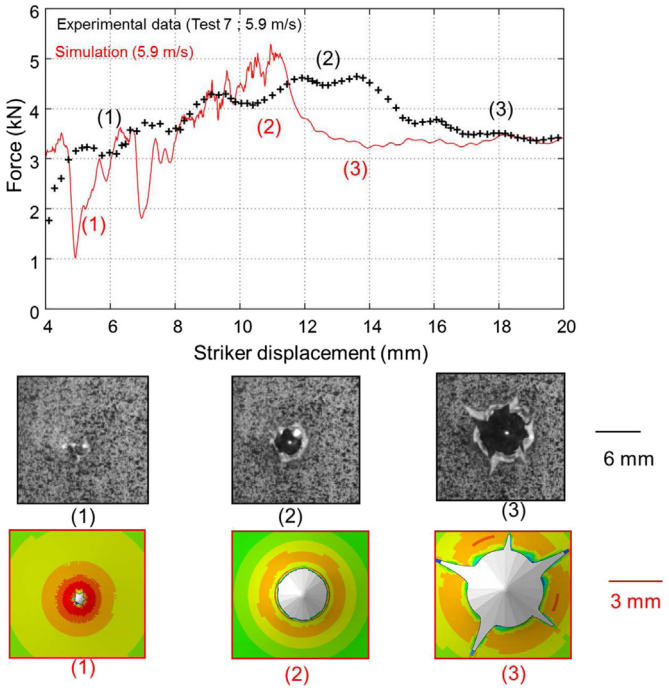

Fig. 20. Second peak force as a function of the time for a 13 kg striker and 2 mm thick plates (test 7) at $V_0 = 5.9$ m/s (FE simulation vs experimental data).

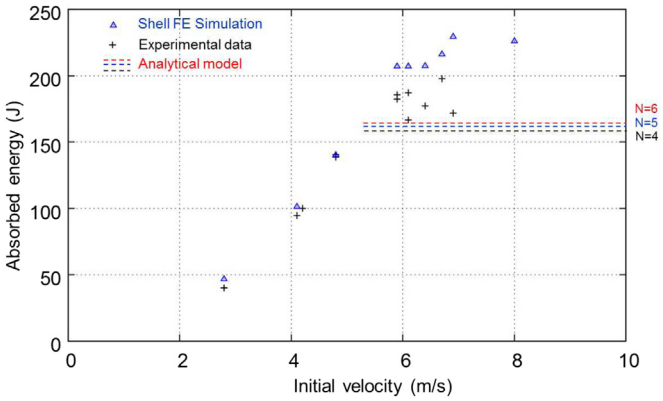

Fig. 21. Absorbed energy as a function of the initial velocity (Experimental data vs analytical and FE models).

center of the plate and the force loses its linearity. The shock wave comes back in the center of the plate to perturb the stress (Fig. 19b. (3)). Thus, the force starts to oscillate (Fig. 19a blue point). This phenomenon is then amplified and produces a high drop of force (Fig. 19a grey point) and of stress in the center of the plate (Fig. 19b. (4)). This phenomenon is stopped when the damage starts in the center of the plate (Fig. 18).

After the first peak force, a constant rise of force occurs until a change of the slope of the curve (Fig. 20 (1)). At this time, in the simulation, the striker starts to appear on the other side of the plate. The curve of force continues to rise until the second peak force is reached (Fig. 20 (2)). When the peak force is reached, cracks begin to propagate with a high velocity and so the force drops (Fig. 20 (3)). The more petals bend the more their size increase. The energy needed for petals to bend rises. Thus, a size of crack above, the curve of force starts to increase again.

The crack propagates and the force rises until the last peak force. When the maximum force is reached, the striker totally perforates the plates. Then during the fall of the force, it goes trough the petals.

4.3. Energetic results

The analytical model for perforation is an energetic based model. In Fig. 21, the total energy of perforation calculated with the analytical model is plotted for a number of petals equals to 4, 5 and 6. In this figure, the simulated and experimental absorbed energy are plotted as a function of initial velocity. This energy rises with the initial velocity and saturated around 180 J (experiments) and 210 J (simulation). These levels of energy are closed to the one calculated by the analytical model. For a total perforation (velocity higher than 5.9 m/s), the absorbed energy is constant. Thus, the hypothesis of a constant absorbed energy after perforation is confirmed.

4.4. Analysis around the crack tip

Simulations results permit to analyse the mode of crack propagation. A perforation test with an initial velocity of 6.1 m/s is used here. The stress in the plate is plotted in a cylindrical coordinate system (r,θ,z). Fig. 22(a) shows simulations results, in terms of orthoradial stress $\sigma_{\theta\theta}$, at time 4 ms after the impact. The orthoradial stress is the stress normal to the radius of the plate. It can be noticed that the majority of orthoradial stress is condensed in the 5 crack tips. In a chosen element of a crack tip at time 5.7 ms, radial, orthoradial, shear and longitudinal stresses are plotted as a function of time (Fig. 22(b)). In the graph, when fracture occurs around 5.7 ms, the predominant stress is the orthoradial stress. It can be concluded that the fracture mode during petalling is mode I.

The crack number on the simulations evolves between 4 and 5. The mean crack velocity is calculated on FE simulations as the final length of the crack divided by the time of crack propagation. In Fig. 23, the mean crack velocity is compared for numerical and experimental results as a function of the initial velocity. A good agreement is observed, an augmentation of the mean crack velocity with the initial velocity.

5. Conclusion and remarks

Twenty three perforation drop tests are performed on 2024-AA plates (thickness 2 mm and 4 mm) with a 30° conical striker. For the 2 mm thick plate, the ballistic limit velocity is between 4.8 m/s and 5.9 m/s. The number of petals after perforation is between 4 and 6. Looking at the force, three peaks are observed. The first one is just after impact and its value is about 0.5–1.5 kN. When the second peak occurs (about 5 kN), cracks start to propagate. The last peak corresponds to a total perforation of the plate, where the striker passes through the plate. For 4 mm thick plates, the experimental

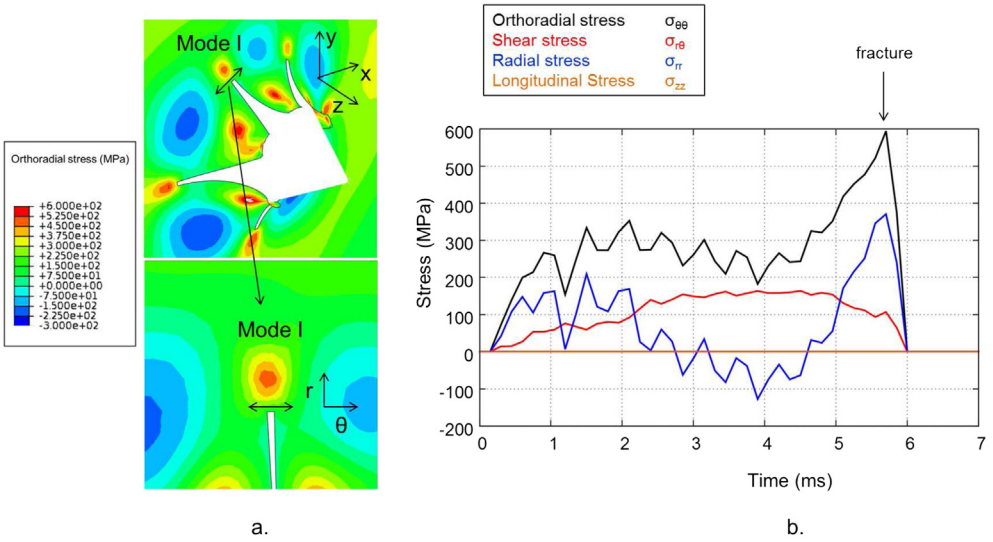

Fig. 22. Picture of the orthoradial stress during simulation ($V_0 = 6.1$ m/s) (a) and evolution of orthoradial, shear, radial and longitudinal stresses as a function of time in an element at the crack tip (b).

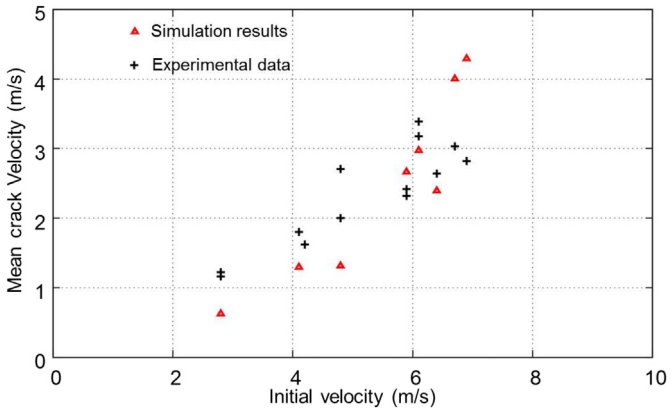

Fig. 23. Mean crack velocity as a function of initial velocity for drop tests and simulations.

setup is not energetically sufficient to involve a complete perforation and the first peak force is not observed.

Two models are presented for the perforation of thin plates. An analytical model is based on an energetic approach of the perforation considering that the perforation work is the sum of the bending elastic work, the bending plastic work the stretching plastic work, the petals' bending work, and the fracture work. This model gives good results in term of residual velocity and absorbed energy. For a 2 mm thick plate, the predicted ballistic limit velocity is respectively 5.0 m/s, 5.0 m/s and 5.1 m/s for 4, 5 or 6 petals. For a 4 mm thick plate, it's about 9.2−9.4 m/s.

The second model is a FE numerical model. The plate is modelled with shell FE associated with a Johnson−Cook behaviour law for AA 2024. Parameters from the literature are calibrated in order to fit the experimental crack velocity. One of the damage law parameter (D_1) is modified according to a simplified model of perforation with an imposed crack velocity. Thus good results in term of force and velocity are obtained. The simulation reproduces the three peaks of force. The first peak is due to the propagation of the shock wave in the plate. The second peak is justified by the fact that the striker start to perforate the plate and cracks are propagating with a high velocity. The last peak occurs when the plate is totally perforated. For 2 mm thick plate, a study on crack propagation permits to conclude that the principal mode of fracture is the traction mode I.

Acknowledgement

This work is a part of the FUI (French government funding agency) BELOCOPA project. The financial support of this work from OSEO, a structure for the benefit of SMEs and innovation, is gratefully acknowledged.

References

[1] Abaqus. Abaqus analysis user's manual. Karlsson, and Sorensen. USA: Dassault Systmes; September 2010.
[2] Atkins A, Khan MA, Liu J. Necking and radial cracking around perforations in thin sheets at normal incidence. Int J Impact Eng 1998;21(7):521−39.
[3] Awerbuch J, Bodner S. Analysis of the mechanics of perforation of projectiles in metallic plates. Int J Solids Struct 1974;10(6):671−84.
[4] Borvik T, Clausen AH, Hopperstad OS, Langseth M. Perforation of AA5083-h116 aluminium plates with conical-nose steel projectiles experimental study. Int J Impact Eng 2004;30(4):367−84.
[5] Borvik T, Hopperstad O, Berstad T. On the influence of stress triaxiality and strain rate on the behaviour of a structural steel. part ii. numerical study. Eur J Mech A/Solids 2003;22(1):15−32.
[6] Borvik T, Olovsson L, Dey S, Langseth M. Normal and oblique impact of small arms bullets on AA6082-t4 aluminium protective plates. Int J Impact Eng 2011;38(7):577−89.
[7] Clifton RJ. Response of materials under dynamic loading. Int J Solids Struct 2000;37(1−2):105−13.
[8] Combescure A, Coret M, Elguedj T, Cazes F, Haboussa D. Cohesive laws X-FEM association for simulation of damage fracture transition and tensile shear switch in dynamic crack propagation. Procedia 2012;3(0):274−91. IUTAM Symposium on Linking Scales in Computations: from Microstructure to Macro-scale properties.
[9] Dean J, S-Fallah A, Brown P, Louca L, Clyne T. Energy absorption during projectile perforation of lightweight sandwich panels with metallic fibre cores. Compos Struct 2011;93(3):1089−95.
[10] Elek P, Jaramaz S, Mickovi D. Modeling of perforation of plates and multi-layered metallic targets. Int J Solids Struct 2005;42(34):1209−24.
[11] Forrestal M, Luk V, Rosenberg Z, Brar N. Penetration of 7075-t651 aluminum targets with ogival-nose rods. Int J Solids Struct 1992;29(1415):1729−36.
[12] Grytten F, Borvik T, Hopperstad O, Langseth M. Low velocity perforation of AA5083-H116 aluminium plates. Int J Impact Eng 2009;36(4):597−610.
[13] Grytten F, Fagerholt E, Auestad T, Forre B, Borvik T. Out-of-plane deformation measurements of an aluminium plate during quasi-static perforation using structured light and close-range photogrammetry. Int J Solids Struct 2007;44(17):5752−73.
[14] Hakim V, Karma A. Laws of crack motion and phase-field models of fracture. J Mech Phys Solids 2009;57(2):342−68.
[15] Hodowany J, R G, R. AJ, R P. Partition of plastic work into heat and stored energy. J Exp Mech 2000;40:113−23.
[16] Hou S, Li Q, Long S, Yang X, Li W. Multiobjective optimization of multi-cell sections for the crashworthiness design. Int J Impact Eng Nov. 2008;35(11):1355−67.
[17] Iqbal M, Chakrabarti A, Beniwal S, Gupta N. 3d numerical simulations of sharp nosed projectile impact on ductile targets. Int J Impact Eng 2010;37(2):185−95.
[18] Irwin. Analysis of stresses and strains near the end of a crack traversing a plate. J Appl Mech 1957;24.
[19] Jackson KE, Boitnott RL, Fasanella EL, Jones LE, Lyle KH. A history of full-scale aircraft and rotorcraft crash testing and simulation at nasa langley research center. In: 4th Triennial International Aircraft and Cabin Safety Research Conference. Philadelphia, Pennsylvania, USA: NASA Langley Research Center; 2004. p. 22.
[20] Johnson GR, Cook WH. A constitutive model and data for metals subjected to large strains, high strain rates and high temperatures. In: Proceedings of the 7th international symposium on ballistics, Seventh International Symposium on Ballistics, 547(11). The Hague, Netherlands: American Defense Preparedness Association; 1983. p. 541−7.
[21] Johnson GR, Cook WH. Fracture characteristics of three metals subjected to various strains, strain rates, temperatures and pressures. Eng Fract Mech 1985;21(1):31−48.
[22] Jones D, Poulose P, Eftis J, Liebowitz H. Gc and r-curve fracture toughness values for aluminum alloys under plane stress conditions. Eng Fract Mech 1978;10(3):433−52.
[23] Kpenyigba K, Jankowiak T, Rusinek A, Pesci R. Influence of projectile shape on dynamic behavior of steel sheet subjected to impact and perforation. Thin-Walled Struct 2013;65(0):93−104.
[24] Landkof B, Goldsmith W. Petalling of thin, metallic plates during penetration by cylindro-conical projectiles. Int J Solids Struct 1985;21(3):245−66.
[25] Lesuer DR. Experimentel investigations of material models for Ti 6Al 4V titanium and 2024-t3 aluminum. Washington: Office of Aviation Research; 2000. p. 1−41.
[26] Macek RW, Silling SA. Peridynamics via finite element analysis. Finite Elem Analysis Des 2007;43(15):1169−78.
[27] Nazeer MM, Khan M, Naeem A, ul Haq A. Analysis of conical tool perforation of ductile metal sheets. Int J Mech Sci 2000;42(7):1391−403.
[28] Neugebauer R, Bouzakis K-D, Denkena B, Klocke F, Sterzing A, Tekkaya A, et al. Velocity effects in metal forming and machining processes. CIRP Ann - Manuf Technol 2011;60(2):627−50.
[29] Prabel B. Modelisation avec la methode X-FEM de la propagation dynamique et de l'arret de fissure de clivage dans un acier de cuve REP. Lyon: INSA; 2007. p. 188 [Ph.D. thesis].
[30] Ramezani M, Ripin ZM. Combined experimental and numerical analysis of bulge test at high strain rates using split hopkinson pressure bar apparatus. J Mater Process Technol 2010;210(8):1061−9.
[31] Ren Z, Ru C. Numerical investigation of speed dependent dynamic fracture toughness of line pipe steels. Eng Fract Mech 2013;99(0):214−22.
[32] Rodriguez-Martinez J, Rusinek A, Arias A. Thermo-viscoplastic behaviour of 2024-t3 aluminium sheets subjected to low velocity perforation at different temperatures. Thin-Walled Struct 2011;49(7):819−32.
[33] Tassin A. Modélisation tridimensionnelle d'impacts hydrodynamiques pour l'étude du tossage des bulbes d'étrave [Ph.D. thesis]. Brest: Universit de Bretagne Occidentale; 2010. p. 213.
[34] Wierzbicki T. Petalling of plates under explosive and impact loading. Int J Impact Eng 1999;22(910):935−54.
[35] Woodward R, de Morton M. Penetration of targets by flat-ended projectiles. Int J Mech Sci 1976;18(3):119−27.
[36] Xiong Y. Toute la resistance des materiaux − Formulaire. 2006. p. 910. Shu Book.
[37] Xu X-P, Needleman A. Numerical simulations of fast crack growth in brittle solids. J Mech Phys Solids 1994;42(9):1397−434.